Exp Fluids (2012) 53:1713–1722
DOI 10.1007/s00348-012-1382-5

RESEARCH ARTICLE

# Hot-wire spatial resolution effects in measurements of grid-generated turbulence

**A. Ashok · S. C. C. Bailey · M. Hultmark · A. J. Smits**

Received: 9 December 2011 / Revised: 29 August 2012 / Accepted: 30 August 2012 / Published online: 27 September 2012


**Abstract** We use grid-generated turbulence as a benchmark flow to test the effects of spatial resolution on turbulence measurements with hot wires. To quantify the spatial filtering, measurements of the turbulence statistics and spectra downstream of the grid were made using hot wires of varying length and compared to the results from a new nanoscale thermal anemometry probe, which has a sensing length of the order of, or smaller than, the Kolmogorov scale. In order to separate the effects of temporal and spatial filtering, a study was performed to ensure that the data were free of the artifacts of temporal filtering so that differences in the measurements could be wholly attributed to spatial filtering. An empirical correlation for the attenuation of the streamwise Reynolds stress due to spatial filtering is constructed, and it is shown that these grid turbulence results relate directly to the near-wall region of wall-bounded flows, where the effects of spatial filtering are most acutely felt. The effect of spatial filtering on the streamwise spectrum function is observed to extend to almost all wavenumbers, even those significantly lower than the length of the hot wire itself. It is also shown that estimates of the Kolmogorov scale are affected by spatial filtering when wires longer than the Kolmogorov length are used.

A. Ashok (✉) · M. Hultmark · A. J. Smits
Department of Mechanical and Aerospace Engineering, Princeton University, Princeton, NJ, USA
e-mail: aashok@princeton.edu

S. C. C. Bailey
Department of Mechanical Engineering, University of Kentucky, Lexington, KY, USA

## 1 Introduction

A well-known source of experimental error in hot-wire anemometry measurements of turbulence is the spatial filtering of velocity fluctuations, which occurs when the sensing length of the probe, $\ell$, is larger than the smallest turbulence length scale, the Kolmogorov length $\eta$. As summarized by McKeon et al. (2007), this spatial filtering problem has been the subject of considerable analytical and experimental investigation, dating back to Dryden (1937).

Whereas most analytical approaches to spatial filtering have been limited to the statistically simple flow of homogeneous and isotropic turbulence, many flows of practical interest are inhomogeneous and anisotropic. In these cases, investigations of spatial filtering are typically experimental or numerical in nature, with notable studies for wall-bounded flows by Ligrani and Bradshaw (1987), Hutchins et al. (2009), Chin et al. (2009), Cameron et al. (2010) and Smits et al. (2011). These investigations all assume that the viscous length describes the smallest turbulence length scale, where the viscous length is defined as $\nu/u_\tau$ with $u_\tau$ the friction velocity and $\nu$ the kinematic viscosity. They therefore focus on $\ell^+$ as the primary parameter governing spatial filtering, where $\ell^+ = \ell u_\tau/\nu$, although Smits et al. identified the parameter $\ell/y$ as an important factor outside the near-wall region.

Here we use measurements of turbulence generated by a grid, acquired using a range of hot-wire sensor lengths at a series of streamwise distances downstream of the grid, to investigate the impact of spatial filtering on measurements of the turbulence statistics. We compare the results from these conventional probes to those from a new Nano-Scale Thermal Anemometry Probe (NSTAP) (see Bailey et al. (2010) and Vallikivi et al. (2011)). As the NSTAP sensing length is smaller than the Kolmogorov scale for almost all

cases considered (and at most only 20 % larger than the Kolmogorov scale) for the purposes of the current experiment, the NSTAP provides a reference datum to which the conventional probes can be compared. Points of comparison include streamwise evolution of the turbulence intensity as well as the turbulent spectra and estimates of the Kolmogorov length scales. Additionally, we relate the spatial filtering observed in the grid-generated turbulence to that seen in the near-wall region of wall-bounded turbulence and thereby provide a framework for the effects of spatial filtering that covers homogeneous and inhomogeneous flows.

Furthermore, increasing the length of the wire has the additional undesired effect of reducing the frequency response of the wire. This has the potential danger of introducing temporal filtering due to inadequate frequency response. We show that the data taken here are free of the effects of temporal filtering, at least in the statistics considered here, and we therefore make the case that any differences between the wires may be attributed to the effects of spatial filtering alone.

## 2 Experimental methods

The grid turbulence was generated in a low-speed, 0.6 m × 0.9 m, closed-circuit wind tunnel using an $M = 6.4$ mm square mesh grid with 45 % solidity, located at the test section inlet. The probes were mounted on the wind tunnel centerline at positions $20M \leq x \leq 90M$ downstream of the grid. At each measurement position, time histories of streamwise velocity, $U(t)$, were acquired for each probe at a rate of 80 kHz for 60 s. Tests were conducted at two free-stream velocities, $\overline{U} = 10$ and 30 m/s, corresponding to $Re_M = \overline{U}M/\nu$ of 4,300 and 12,800, respectively. The corresponding range of Kolmogorov length scales ranged from 0.04 to 0.275 mm, and the integral length scales varied from about $0.1M$ to $0.3\ M$ depending on probe location and flow velocity. The Reynolds number based on the Taylor microscale, $Re_\lambda$, was estimated to be between 30 (for $x/M = 90$ and $Re_M = 4{,}300$) and 80 (for $x/M = 20$ and $Re_M = 12{,}800$).

Probe calibrations were performed with the grid removed from the wind tunnel before and after each measurement using a combination of Pitot and static pressure probes for the velocity reference. Calibration data were fitted using a fourth-order polynomial. If the difference between the calibration curves before and after each measurement was larger than 5 % in velocity, then the measurement was discarded. The tunnel temperature was regulated to better than 0.25°C for any given measurement, and therefore, no temperature correction was deemed necessary.

Two types of thermal anemometry probes were used in this study: a new Nano-Scale Thermal Anemometry Probe (NSTAP) and standard hot-wire probes, which together covered a range of $\ell/\eta$ of between 0.1 and 80. The NSTAP probe used in this study was manufactured using standard semi-conductor manufacturing techniques, as outlined in Vallikivi et al. (2011), who have also validated the NSTAP performance in both grid-generated turbulence and pipe flow. The sensor used here is a free-standing 60-μm-long element, measuring 100 nm by 2 μm in cross section, suspended between two aerodynamic support structures. These probes were operated using a Dantec Streamline constant temperature anemometry (CTA) system in 1:1 bridge mode, resulting in a square wave frequency response $f_{sq}$ exceeding 150 kHz.

The hot-wire probes used here were single-wire, normal probes. They were manufactured by etching Wollaston wire of 2.5 and 1.25 μm in diameter (90 % Pt 10 % Rh) to produce sensing lengths ranging from 0.25 to 4 mm, so that $200 \leq \ell/d \leq 1{,}600$, where $d$ is the wire diameter. The length-to-diameter ratio $\ell/d$ has classically been used to quantify end conduction effects, and Ligrani and Bradshaw (1987)'s criterion for $\ell/d > 200$ has been adhered to in this experiment. Hultmark et al. (2011) have suggested a new criterion for end conduction effects in hot wires, which takes into account the effect of wire thermal conductivity, Reynolds number and temperature overheat ratio in addition to the length-to-diameter ratio. Their criterion, where it is required that $\frac{\ell}{d}\sqrt{4a\left(\frac{k_f}{k}\right)Nu} > 14$, is also satisfied in the current investigation. Here, $a$ is the resistance ratio ($\overline{R}/R_0$), where $R_0$ is the resistance of the wire at ambient conditions and $\overline{R}$ is the hot resistance, $k_f$ the thermal conductivity of the fluid, $k$ the thermal conductivity of the wire material and $Nu$ the Nusselt number. The hot wires were operated in the same CTA system as the NSTAP at wire temperatures typically between 290 and 370°C.

For each combination of sensor length and free-stream velocity, the temperature overheat ratio and corresponding square wave frequency response are summarized in Table 1. The NSTAP and 0.25-mm wire were run at a lower temperature overheat ratios of 1.3 and 1.6, respectively. In the case of the 0.25-mm wire, this was done to minimize calibration drift, most likely caused by hot spots along the 1.25-μm-diameter wire. In the case of the NSTAP, it has been found that the NSTAP will burn out when operated in CTA mode at higher overheats, for reasons that are not yet clear.

## 3 Flow results

In the initial period of decay, the turbulent kinetic energy in grid turbulence decays according to a power law so that,

**Table 1** Temperature overheat ratio $R$, as well as square wave frequency response, $f_{sq}$, and Kolmogorov frequency, $f_K$, in kHz for each probe and flow tested

| $Re_M$ | NSTAP 0.06 (mm) | HW 0.25 (mm) | HW 0.5 (mm) | HW 1 (mm) | HW 2 (mm) | HW 4 (mm) |
|---|---|---|---|---|---|---|
| | $R = 1.3$ | 1.6 | 2.1 | 2 | 1.9 | 1.85 |
| 4,300 | $f_{sq} = 90$ | 90 | 50 | 40 | 30 | 15 |
| 4,300 | $f_K = 118$ | 118 | 118 | 118 | 118 | 118 |
| 12,800 | $f_{sq} = 150$ | 120 | 75 | 60 | 50 | 25 |
| 12,800 | $f_K = 847$ | 847 | 847 | 847 | 847 | 847 |

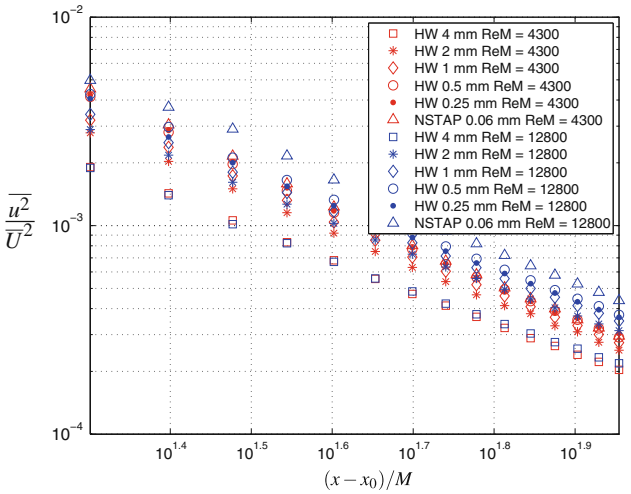


**Fig. 1** Variance of streamwise velocity as a function of downstream distance. Measurements performed at $Re_M = 4{,}300$ are shown in *red* and those taken at $Re_M = 12{,}800$ are shown in *blue*

assuming homogeneous isotropic conditions, the variance of the streamwise velocity fluctuations, $\overline{u^2}$, is expected to decay according to

$$\frac{\frac{3}{2}\overline{u^2}}{\overline{U}^2} = A\left(\frac{x - x_0}{M}\right)^{-n} \tag{1}$$

where $n$ and $A$ are constants that depend on the nature of the grid, and $x_0$ is the virtual origin of the turbulence decay.

Figure 1 shows the streamwise variation of $\frac{\overline{u^2}}{\overline{U}^2}$ as measured by each of the probes used in this study. As expected, the values measured by long sensors are lower than the values measured with shorter sensors due to spatial filtering effects, and as the sensing length decreases, the agreement among the measurements improves.

Table 2 summarizes the values of $n$ and $A$ for $x_0/M = 3$ in Eq. 1 found from each of the probes used in this study. For the high Reynolds number NSTAP measurements, $n$ lies within the expected range of $1.15 < n < 1.45$ cited by Pope (2007). For the lower Reynolds number case, however, $n$ was found to be outside the expected range, indicating a possible deviation from canonical homogeneous and isotropic turbulent conditions. The general trend of decreasing exponent in both cases can be attributed to reduction in $\overline{u^2}$ due to spatial filtering, the magnitude of which will decrease as $x/M$ increases and the Kolmogorov length scale grows.

To estimate the Kolmogorov scale, the turbulent dissipation rate, $\varepsilon$, was estimated in two ways. First, the dissipation rate was computed from the gradient of the variance according to:

$$\varepsilon_1 = -\overline{U}\frac{d}{dx}\left(\frac{3}{2}\overline{u'^2}\right) \tag{2}$$

This method for estimating dissipation rate relies on an assumption of large-scale homogeneity and isotropy which, as indicated above, may not hold for the low Reynolds number case. Second, the dissipation rate was computed by integrating the dissipation spectrum, as given by Tennekes and Lumley (1972):

$$\begin{aligned}\varepsilon_2 &= \int_0^\infty D(k)\mathrm{d}k \;\approx\; 15\nu\int_0^\infty k^2E(k)\mathrm{d}k \\ &= 15\nu\int_0^\infty k^3E(k)\mathrm{d}(log(k)).\end{aligned} \tag{3}$$

**Table 2** Coefficients of the power decay law given by Eq. 1 determined over the full range of data (from $x/M = 20$ to 90) for all probes

| | Coefficients | NSTAP 0.06 (mm) | HW 0.25 (mm) | HW 0.5 (mm) | HW 1 (mm) | HW 2 (mm) | HW 4 (mm) |
|---|---|---|---|---|---|---|---|
| $Re_M = 4{,}300$ | $n$ | 1.69 | 1.65 | 1.64 | 1.55 | 1.50 | 1.40 |
| | $A$ | 0.560 | 0.460 | 0.435 | 0.273 | 0.203 | 0.104 |
| $Re_M = 12{,}800$ | $n$ | 1.40 | 1.47 | 1.50 | 1.41 | 1.39 | 1.34 |
| | $A$ | 0.27 | 0.25 | 0.30 | 0.19 | 0.16 | 0.08 |

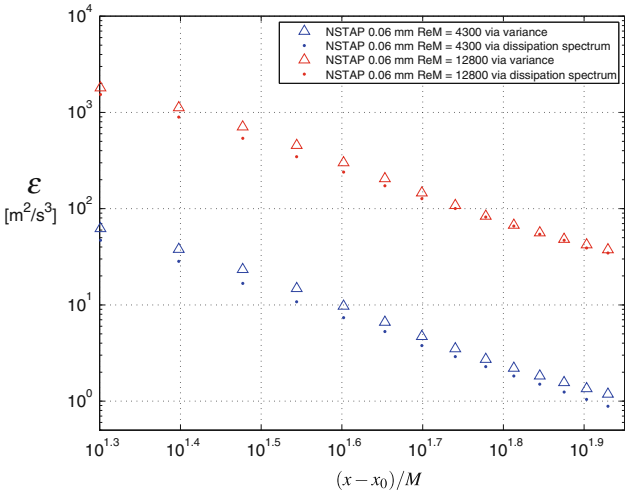


**Fig. 2** Dissipation rates, $\varepsilon_1$ and $\varepsilon_2$, plotted as a function of downstream position for $Re_M = 4{,}300$ and $Re_M = 12{,}800$

This calculation relies on an assumption of small-scale isotropy, which is somewhat less restrictive in flows with large-scale anisotropy.

Figure 2 shows that there is a 5–25 % difference between $\varepsilon_1$ and $\varepsilon_2$, depending on the downstream location. Also, $\varepsilon_2$ is consistently smaller than $\varepsilon_1$ because the integration needed to be truncated at $f = 20$ kHz due to significant anemometer noise at the highest wavenumbers. For consistency, $\varepsilon_1$ will be used for the rest of the paper unless otherwise stated. The effect on scaling, which is the most critical aspect for the purposes of this paper, is minimal in that the Kolmogorov length scale derived using $\varepsilon_1$ or $\varepsilon_2$ differs by less than about 5 %. $\eta$ is proportional to $\varepsilon$ in power 1/4, so that a 100 % error in $\varepsilon$ only amounts to a 19 % error in $\eta$

## 4 Temporal Filtering

It is important to distinguish between the effects of temporal filtering, due to inadequate frequency response, and spatial filtering, due to spanwise averaging over the length of the wire. It is necessary to identify the data that are free of temporal filtering so that the effects of spatial filtering can be clearly separated from those of temporal filtering. In this respect, we will use the NSTAP results as a standard for comparison, since for all NSTAP measurements $\eta/\ell > 1$ and so can be considered to be free of spatial filtering effects under all conditions.

The highest frequency motion encountered by the probe is given by the mean velocity carrying the smallest motion past the probe. We call this the Kolmogorov frequency $f_K$, given by $f_K = \overline{U}/\eta$. Ideally, the frequency response of the wires used in this investigation needs to be higher than $f_K$ for all cases. As shown in Tables 3 and 4, this is a severe requirement. A more pragmatic requirement would be to have a sufficient frequency response to resolve, for example, the variance, the dissipation rate and the Kolmogorov length scale to a specified degree of accuracy.

In order to do so, we note that the frequency response inferred using a square wave test, $f_{sq}$, corresponds to the −3dB point, where the power is already reduced by 50 %. In addition, if the system response can be approximated as second order, the response at other frequencies depends crucially on the damping ratio (see Fig. 3). In adjusting the frequency response in our experiments, we maintained the system response as close as possible to that of a critically damped system such as that shown for the second-order system response corresponding to $\zeta = 0.6$ in Fig. 3. Then the frequency at which the gain differs from unity by less than 5 % corresponds approximately to 0.65 $f_{sq}$.

Figure 4 shows the cumulative integral of the velocity spectra for all the data taken using the NSTAP. To recover 99 % of the variance, we see that it is necessary to have a flat frequency response up to about 5.3 kHz for $Re_M = 4{,}300$, and 17.1 kHz for $Re_M = 12{,}800$.

Similarly, the dissipation rate $\varepsilon_1$ (see Eq. 2) and the Kolmogorov length scale are shown as a function of frequency in Figs. 5 and 7 respectively. For $\varepsilon_1$ (plotted in Fig. 5), we find that a frequency response of about 6 kHz is required for $Re_M = 4{,}300$ and about 17.1 kHz for

**Table 3** The frequency response in kHz required to measure the variance, dissipation rate and Kolmogorov length scale within 1 % at $x/M = 20$ is shown for all probes at $Re_M = 4{,}300$

| | NSTAP 0.06 (mm) | HW 0.25 (mm) | HW 0.5 (mm) | HW 1 (mm) | HW 2 (mm) | HW 4 (mm) |
|---|---|---|---|---|---|---|
| $\overline{u^2}$ | 5.3 | 5.3 | 4.6 | 4.6 | 4.6 | 3.6 |
| $\varepsilon_1$ | 6.0 | 6.0 | 5.3 | 5.3 | 5.3 | 3.1 |
| $\varepsilon_2$ | 13.2 | 13.2 | 13.2 | 13.2 | 11.6 | 11.6 |
| $\eta$ | 4.1 | 3.6 | 3.6 | 3.6 | 3.1 | 2.1 |
| $f_{sq}$ | 90 | 90 | 50 | 40 | 30 | 15 |
| $0.65f_{sq}$ | 58 | 58 | 32 | 26 | 19 | 9 |

Here, $\varepsilon_1$ and $\varepsilon_2$ are obtained using Eqs. 2 and 3, respectively, and $\eta$ was found using $\varepsilon_1$. The square wave frequency response $f_{sq}$ and $0.65f_{sq}$ are also shown for comparison

**Table 4** Same as Table 3 but for $Re_M = 12{,}800$

| | NSTAP 0.06 (mm) | HW 0.25 (mm) | HW 0.5 (mm) | HW 1 (mm) | HW 2 (mm) | HW 4 (mm) |
|---|---|---|---|---|---|---|
| $\overline{u^2}$ | 17.1 | 17.1 | 17.1 | 17.1 | 15.0 | 11.6 |
| $\varepsilon_1$ | 17.1 | 17.1 | 17.1 | 17.1 | 17.1 | 17.1 |
| $\varepsilon_2$ | 37.5 | 37.5 | 37.5 | 33.0 | 33.0 | 33.0 |
| $\eta$ | 15.0 | 15.0 | 15.0 | 13.2 | 11.6 | 8.9 |
| $f_{sq}$ | 150 | 120 | 75 | 60 | 50 | 25 |
| $0.65 f_{sq}$ | 97 | 78 | 49 | 39 | 32 | 16 |

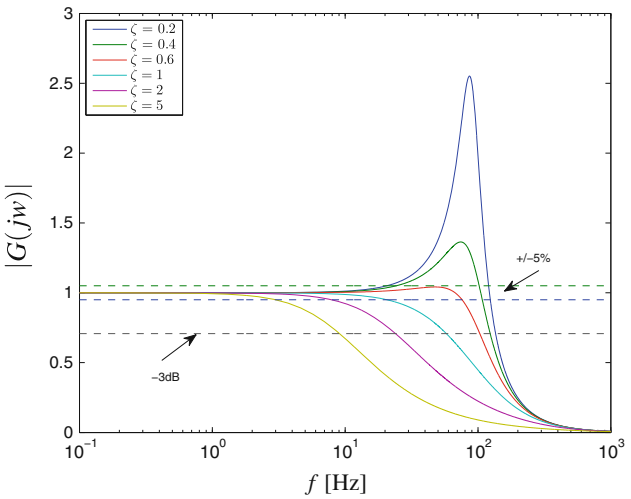


**Fig. 3** Bode diagram for a second-order system with $f$sq = 90 kHz

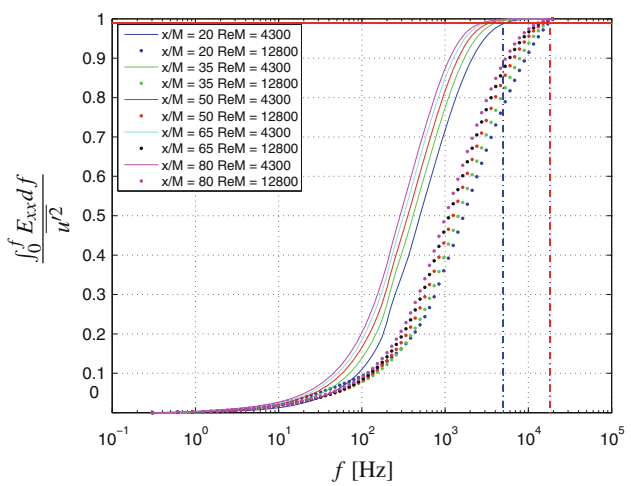


**Fig. 4** Cumulative integral of the variance, normalized by its asymptotic value, as measured by the NSTAP probe. The *dashed-dotted lines* show the approximate frequency at which 99 % of the variance at all locations is captured for $Re_M = 4{,}300$ and $Re_M = 12{,}800$

$Re_M = 12{,}800$ to find $\varepsilon_1$ accurate to within 1 % of the NSTAP-computed value. For $\varepsilon_2$ (see Fig. 6) about 13.2 kHz for $Re_M = 4{,}300$ and 37.5 kHz for $Re_M = 12{,}800$

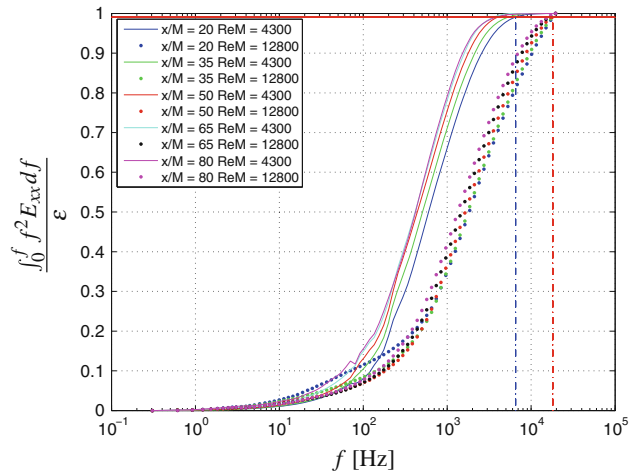


**Fig. 5** Cumulative integral of the dissipation rate $\varepsilon_1$, normalized by its asymptotic value, as measured by the NSTAP probe. *Symbols* as in Fig. 4

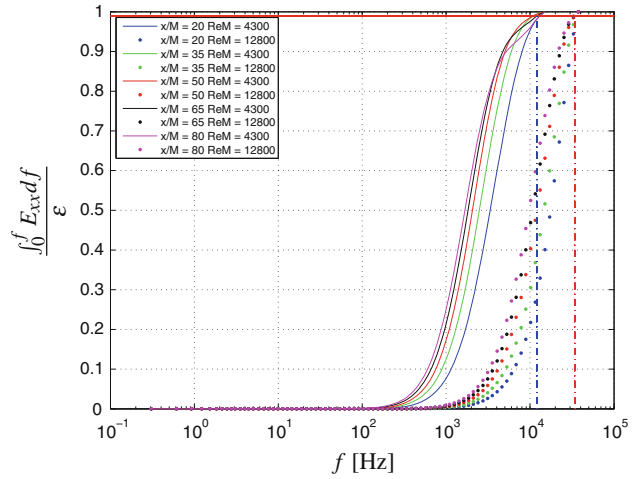


**Fig. 6** Cumulative integral of the dissipation rate $\varepsilon_2$, normalized by its asymptotic value, as measured by the NSTAP probe. *Symbols* as in Fig. 4

is required. For the Kolmogorov length scale, computed using $\varepsilon_2$, the values are 4.1 and 15 kHz, respectively.

The variance, dissipation rate, Kolmogorov length scale and square wave response measured using each probe are summarized in Tables 3 and 4 for the most severe case

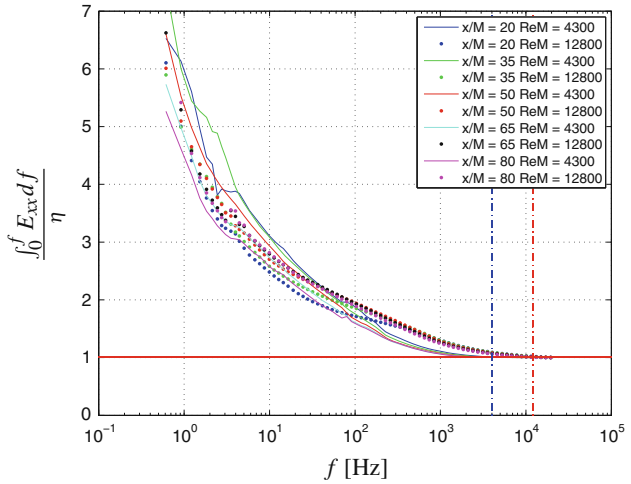


**Fig. 7** Cumulative integral of the Kolmogorov length scale (using $\varepsilon_1$), normalized by its asymptotic value, as measured by the NSTAP probe. *Symbols* as in Fig. 4

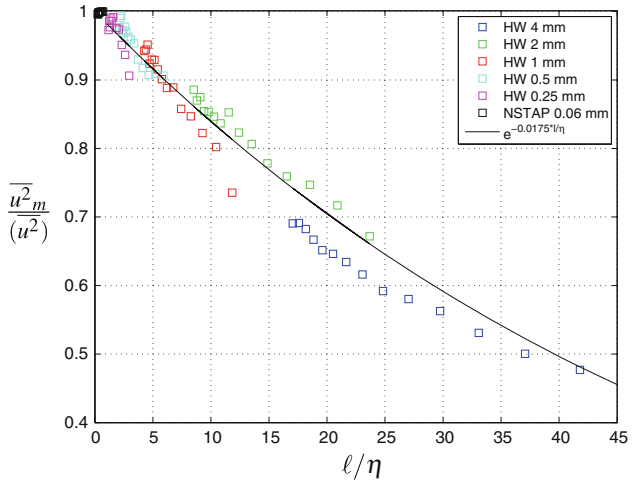


**Fig. 8** The variance measured by the hot wires, normalized by the NSTAP value, as a function of $\ell/\eta$. The *solid line* is Eq. 4

(closest downstream position). We can see that even at the level of $0.65f_{sq}$, the response exceeds 99 % requirements as determined by the NSTAP. Temporal filtering is therefore negligible for our measurements of the variance, the dissipation rate and the Kolmogorov length scale, except perhaps for the 4-mm wire where some temporal filtering may be affecting our estimate of the dissipation rate.

## 5 Spatial filtering

### 5.1 Variance

To determine the magnitude of spatial filtering experienced on the variance measured by the hot wires, $\overline{u^2}_m$, we compare $\overline{u^2}_m$ to its fully resolved value, $\overline{u^2}$, as measured by the NSTAP. Figure 8 shows how this ratio decreases significantly with increasing $\ell/\eta$. This trend was found to be well described by:

$$\frac{\overline{u^2}_m}{\overline{u^2}} = e^{-0.0175\ell/\eta} \tag{4}$$

Traditionally, wall-bounded turbulent flows have relied on spatial filtering criteria based on $\ell^+$, although one would expect a criteria based on $\ell/\eta$ to be more representative of the spatial filtering process within these flows since $\ell^+$ is a fixed quantity and $\ell/\eta$ varies with distance from the wall. Therefore, to compare the spatial filtering observed in grid-generated turbulence to that observed for a similar $\ell/\eta$ range within a highly inhomogeneous wall-bounded turbulent flow, we use the experimental observation by Yakhot et al. (2010) and Smits et al. (2011) that $\eta^+$ follows inner scaling and is independent of Reynolds number for $z^+ < 100$. Here $\eta^+ = \eta u_\tau/\nu$ and $z^+ = z\, u_\tau/\nu$, where $z$ is the distance from the wall. Using this observation, we can compare the spatial filtering effects in grid turbulence to those in wall-bounded turbulence by comparing the dependence on $\ell^+/\eta^+$ with the dependence only on $\ell^+$.

Smits et al. found that the attenuation of the streamwise turbulence due to spatial filtering in wall-bounded flows was described by

$$\frac{\overline{u^2}}{\overline{u^2}_m} = M(\ell^+) f(z^+) + 1 \tag{5}$$

where $f(z^+)$ is a function based on the attached eddy hypothesis which describes the filtering of eddies that scale with distance from the wall through

$$f(z^+) = \frac{15 + \ln(2)}{z^+ \ln[e^{(15-z^+)} + 1]} \tag{6}$$

The function $M(\ell^+)$ describes the filtering of the wire with respect to the smallest eddies in the flow and can be written as

$$M = \left.\frac{\overline{u^2} - \overline{u^2}_m}{\overline{u^2}_m}\right|_{z^+=15} = \frac{B \tanh(\alpha\ell^+)\tanh(\beta\ell^+ - E)}{\left.\overline{u^2}_m\right|_{z^+=15}} \tag{7}$$

with $B = 6.13$, $\alpha = 5.6 \times 10^{-2}$, $\beta = 8.6 \times 10^{-3}$ and $E = -1.26 \times 10^{-2}$. Smits et al. also suggest that when a measurement at $z^+ = 15$ is unavailable, the simple function

$$M = 0.0091\ell^+ - 0.069 \tag{8}$$

can be used instead of Eq. 7.

Figure 9 compares Eq. 4 to the filtering predicted from Eq. 5 using Eqs. 6 and 8. Each of the nine different profiles shown corresponds to the spatial filtering predicted from

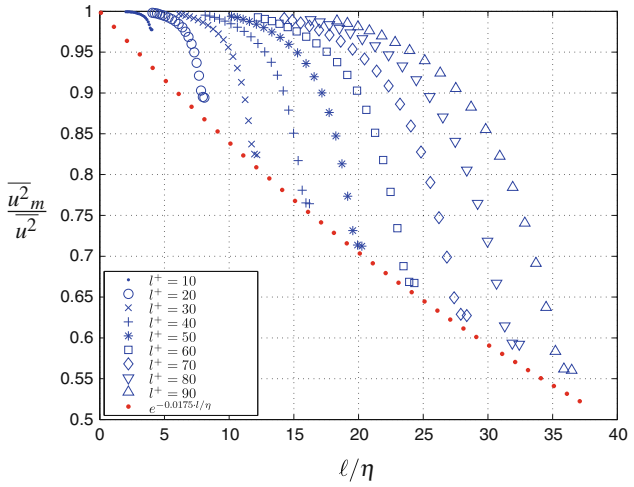


**Fig. 9** Comparison of Eq. 4 (*red dotted line*) found for grid turbulence with Eq. 5 (*blue symbols*) found for wall-bounded flows

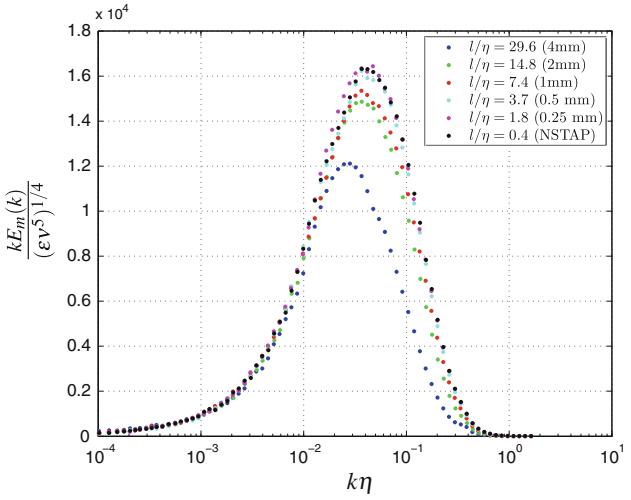


**Fig. 10** Pre-multiplied streamwise wavenumber spectra at $Re_M = 4{,}300$ and $x/M = 40$ plotted in Kolmogorov scaling for a range of $\ell/\eta$

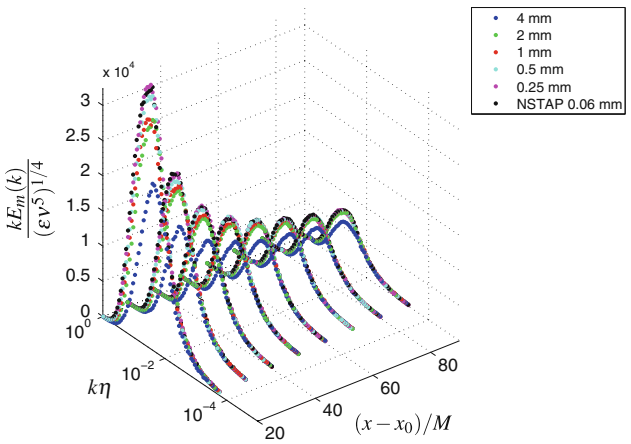


**Fig. 11** Streamwise wavenumber spectra at $Re_M = 4{,}300$ (estimated from frequency spectra) plotted in Kolmogorov scaling for the different downstream positions

Eq. 5 for a single value of $\ell^+$ as $z^+$ is varied from 10 to 100, thus representing a typical near-wall hot wire traverse within a wall-bounded flow. To allow conversion from the wall-bounded flow scaling of $\ell^+$ to the grid turbulence scaling of $\ell/\eta$, we employ the Reynolds number–independent behavior of $\eta^+(z^+)$ observed by Yakhot et al. (2010) and Smits et al. (2011) for $z^+ < 100$. This allows us to find the equivalent value of $\ell/\eta$ at different $z^+$ locations using $\ell^+/\eta^+$. Note that, since Eq. 5 predicts increased spatial filtering as $z^+ \to 0$, in Fig. 9, the lower values of $\overline{u^2}_m/\overline{u^2}$ within a profile correspond to lower values of $z^+$.

As seen in Fig. 9, there is an excellent agreement between the grid-turbulence-based Eq. 4 and the wall-bounded turbulence–based Eq. 5 for the near-wall region ($z^+ < 15$). This result suggests that spatial filtering in the near-wall region of a wall-bounded flow is remarkably similar to the spatial filtering found in grid turbulence, which is a somewhat surprising result because the anisotropy in a wall-bounded flow is highest near the wall. It appears that the scaling with $\ell/\eta$ is more important than the near-wall anisotropy for the single normal hot wire. It is also interesting to note that in wall-bounded flows, as the probe is moved away from the wall, the effect of spatial filtering on $\overline{u^2}_m$ is reduced relative to that found in grid turbulence, perhaps due to an increased proportion of the kinetic energy content contained within the attached eddies, as reflected in Eq. 5.

## 5.2 Spectra

To illustrate the wavenumber dependence of the spatial filtering, the pre-multiplied spectra $kE_m(k)$ at $x/M = 40$ are shown in Fig. 10 for $Re_M = 4{,}300$. Note that the streamwise wavenumber $k$ was estimated from frequency using Taylor's frozen flow hypothesis such that $k = 2\pi\overline{U}/f$. Similar plots for the full range of downstream positions are shown in Fig. 11. All spectra are presented using Kolmogorov scaling, so we expect the spectrum function to be universal at high wavenumber.

In these spectra, the spatial filtering manifests as a reduction in the measured spectrum relative to that measured by the NSTAP. The filtering begins at high wavenumber for small values of $\ell/\eta$, with progressively more aggressive filtering of the energy over an increasing wavenumber range becoming evident as $\ell/\eta$ increases. As Citriniti and George (1997), Cameron et al. (2010) and Chin et al. (2009) and others have noted, the spatial filtering effects manifest at wavelengths much larger than the length of the hot wire due to the one-dimensional filtering of a three-dimensional input.

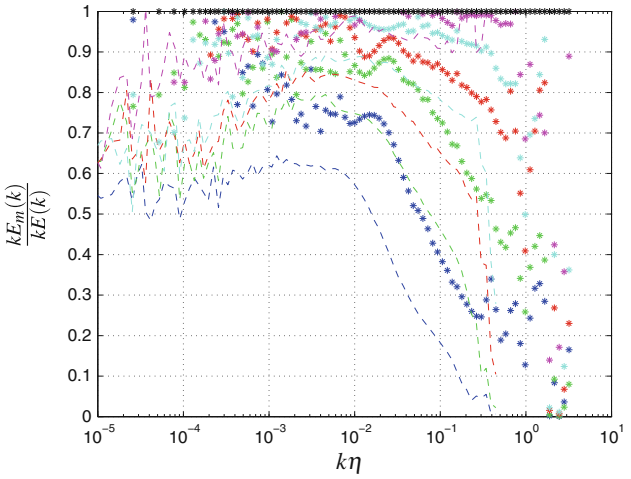


**Fig. 12** Spectra normalized by the NSTAP spectrum at $x/M = 40$ for $Re_M = 4{,}300$ (*solid symbols*) and $Re_M = 12{,}800$ (*dashed lines*) for the different $\ell/\eta$ ratios. *Symbols* as in Fig. 10

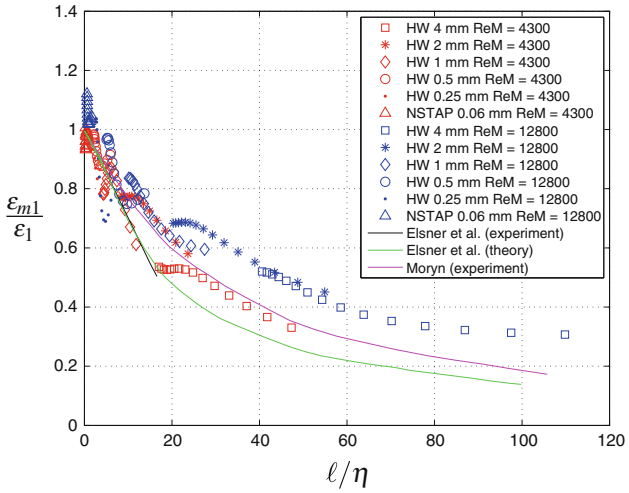


**Fig. 13** The normalized dissipation rate, $\varepsilon_{m1}/\varepsilon_1$, as a function of $\ell/\eta$ for $Re_M = 4{,}300$ and $Re_M = 12{,}800$

Inspection of Fig. 10 suggests that the spectra are fully recovered when $\ell/\eta$ is less than approximately 5. However, when the spectra are normalized by the spectra obtained by the NSTAP, as shown in Fig. 12, we see that only when $\ell/\eta < 2$ is the high wavenumber range fully recovered. In addition, the low-wavenumber filtering is significant with discrepancies on the order of 20 % evident. It may be seen that the effects of spatial filtering extend over the entire wavenumber range once $\ell/\eta$ exceeds approximately 7.

Note that for near-wall measurements performed in wall-bounded shear flow, a limit of $\ell/\eta < 2$ corresponds to a viscous-scaled wire length of $\ell^+ \approx 5$, as noted by Smits et al. (2011), suggesting that the recommendation by Ligrani and Bradshaw (1987) that $\ell^+ < 20$ is insufficient to avoid significant contamination of the measured spectrum by spatial filtering.

As shown in Fig. 12, the magnitude of the spatial filtering occurring in the low-wavenumber range remains relatively constant, whereas there is rapid roll-off of recovered energy once a cutoff wavenumber is exceeded.

### 5.3 Length scales

The energy spectra demonstrate that spatial filtering can have a significant impact on the measured energy content of both the large-scale and small-scale turbulent motions. Here we examine the effect of spatial filtering on measurements of turbulent length scales.

The dissipation rate $\varepsilon_{1m}$ measured by each of the probes, normalized by the value measured by the NSTAP, $\varepsilon_1$, is shown in Fig. 13. The estimated dissipation rate is considerably smaller for the larger probes as would be expected, with as much as 70 % error observed at the highest $\ell/\eta$.

Also shown on Fig. 13 is a curve representing the prediction for spatial filtering effects developed by Elsner et al. (1992) using a Pao spectrum to model the small scales. For $\ell/\eta < 10$ there is good agreement between the present results and the prediction, but for larger values of $\ell/\eta$, there is an increasing deviation from the current results, possibly because the range of $\ell/\eta$ for our results exceeds the range covered by the prediction. Elsner et al. also show results from another (unpublished) experiment by Moryn whose curve-fit coincides very well with the present data, as seen in Fig. 13.

The corresponding estimate of the Kolmogorov length scale, expressed as the measured value normalized by the NSTAP value, $\eta_m/\eta$, is shown in Fig. 14. The results demonstrate a consistent overestimation of the Kolmogorov length scale as $\ell/\eta$ increases, reaching as high as 30 % for the largest probes.

As to the length scales of the energetic scales of turbulence, we consider the streamwise integral length scale, here found by integrating the autocorrelation of $u(t)$ according to

$$L_x = \overline{U}\int_0^\infty \frac{\overline{u(t)u(t-\tau)}}{\overline{u^2}}\mathrm{d}\tau = \overline{U}\int_0^\infty R_{11}(\tau)\mathrm{d}\tau. \qquad (9)$$

where $\tau$ is a time lag.

Example autocorrelations are shown Fig. 15 for all wires. In some of the cases, the autocorrelation function did not pass through zero (most likely due to low-amplitude wind tunnel unsteadiness), and therefore, the integration was performed up to the point where the autocorrelation dropped below a fixed threshold of 0.05. Although this procedure may slightly underestimate $L_x$, it was applied to the data from all probes, so that the comparison across all

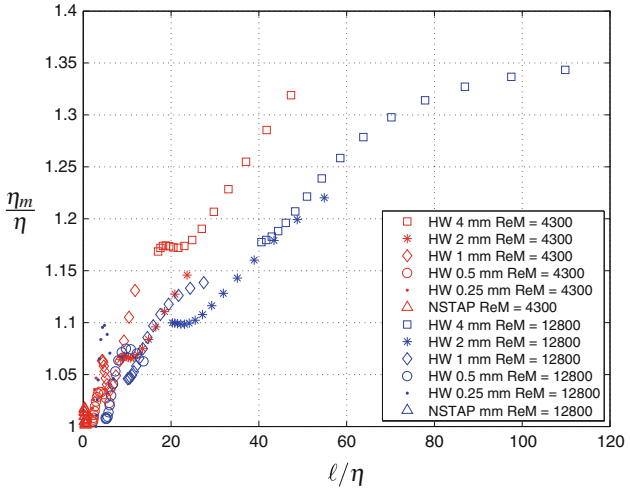


**Fig. 14** Ratio of measured Kolmogorov length scale to the NSTAP measured value, $\eta_m/\eta$, as a function of non-dimensional wire length

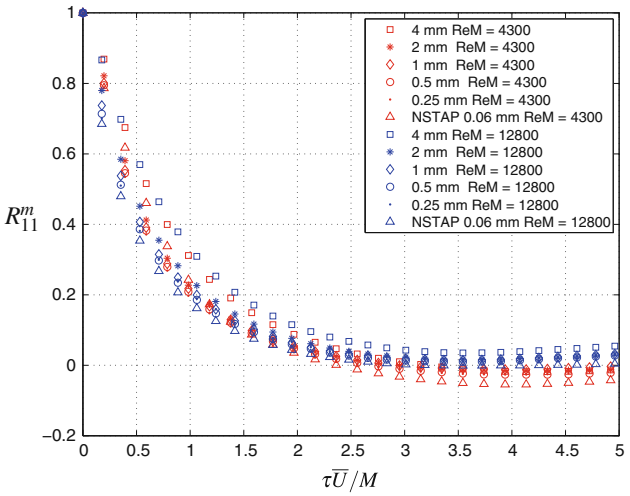


**Fig. 15** Autocorrelation for $x/M = 40$ as measured by all the probes at $Re_M = 4{,}300$ and $Re_M = 12{,}800$

probes is expected to be valid. Consistent with the spectra results, the differences between the probes occur mostly at small displacements, with Fig. 15 indicating that only for the largest wires is there a noticeable deviation from the correlations measured by the NSTAP at longer times. By filtering the small scales of the turbulence, the short-time correlation increases, resulting in an increased integral length scale, was seen in Fig. 16. However, the corresponding estimates of $L_x$, shown in Fig. 16, show that the error in measured integral scale at higher $\ell/\eta$ is as high as 50 %.

The integral scale is directly related to the spectral value at $k = 0$ through $L_x = \pi E(0)/(2\overline{u^2})$ (see Pope (2007)). Figure 12 clearly shows E(0) decreasing with increasing wire length, which should correspond to a decreasing integral scale. However, the net drop in $\overline{u^2}$ is greater than

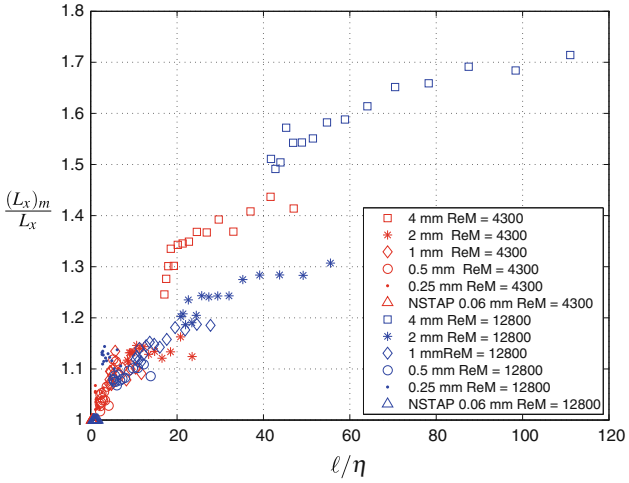


**Fig. 16** The integral length scale, $L_x$, estimated using Eq. 9

that of E(0) causing the integral scale to increase with increasing wire length. This is reflected in the 'kink' shown in Fig. 12.

## 6 Conclusions

Grid turbulence was used to study the effects of spatial filtering on hot-wire measurements of turbulence using conventional wires of varying sensing length and a new MEMS-based velocity sensor, the Nano-Scale Thermal Anemometry Probe, NSTAP. The NSTAP possesses excellent spatial and temporal resolution, and so the results obtained using the NSTAP were assumed to be free of temporal and spatial filtering for all conditions investigated here, and so they provided a standard by which the other probes could be compared.

The measurements by all probes of the variance, the dissipation rate and the Kolmogorov length scale were not affected by temporal filtering, except perhaps for the dissipation measurements by the longest (4 mm long) wire.

Spatial filtering effects were clearly visible in the measurements of the variance, and the energy spectra revealed that the effects of spatial filtering can propagate to almost all wavenumbers and are not limited to wavelengths smaller than the sensing length. A comparison between the present grid turbulence results and the correction for wall-bounded flow proposed by Smits et al. (2011) demonstrated that spatial filtering effects in the anisotropic near-wall region of the wall-bounded flow were similar to those occurring in isotropic grid turbulence.

In grid turbulence, the effects of spatial filtering on estimates of the variance, dissipation rate and Kolmogorov length scale were found to be negligible for probes with $\ell/\eta < 2$. The spectrum at high wavenumber is relatively

well recovered for $\ell/\eta < 2$, although the spectrum is more sensitive to $\ell/\eta$ than the variance. For the near-wall region of a boundary layer ($z^+ < 100$), this criterion corresponds approximately to $\ell^+ < 5$. The corresponding frequency for a motion of size $2\eta$ is $U/(2\eta)$ or $f_K/2$. Since the actual frequency response needed to capture variance and small-scale statistics was found to be closer to $f_K/10$, this result indicates that the spatial criterion is more restrictive than the temporal one which is consistent with the observation that spatial filtering affects all scales whereas temporal filtering affects primarily the energy at higher wavenumbers.

**Acknowledgments** This work was supported by ONR Grant N00014-09-1-0263 (Program Manager Ron Joslin) and NSF Grant CBET-1064257 (Program Manager Henning Winter). Margit Vallikivi provided the NSTAP probes and Mike Vocaturo and Glenn Northey generously gave their technical assistance.

## References

Bailey S, Kunkel G, Hultmark M, Vallikivi M, Hill J, Meyer K, Tsay C, Arnold C, Smits A (2010) Turbulence measurements using a nanoscale thermal anemometry probe. J Fluid Mech 663:160–179

Cameron J, Morris S, Bailey S, Smits A (2010) Effects of hot-wire length on the measurement of turbulent spectra in anisotropic flows. Meas Sci Technol 21:105–407

Chin C, Hutchins N, Ooi A, Marusic I (2009) Use of direct numerical simulation (dns) data to investigate spatial resolution issues in measurements of wall-bounded turbulence. Meas Sci Technol 20:115–401

Dryden HL, Mock GBSGB, Skramstad WC (1937) Measurements of intensity and scale of wind-tunnel turbulence and their relation to the critical reynolds number of spheres. Natl Adv Comm Aeronaut Tech. Rep. 581

Elsner JW, Domagala P, Elsner W (1992) Effect of finite spatial resolution of hot-wire anemometry on measurements of turbulence energy dissipation. Meas Sci Technol 4:517–523

George JCW (1997) The reduction of spatial aliasing by long hot-wire anemometer probes. Exp Fluids 23:217–224

Hultmark M, Ashok A, Smits A (2011) A new criterion for end-conduction effects in hot-wire anemometry. Meas Sci Technol 22:55,401–55,405

Hutchins N, Nickels T, Marusic I, Chong M (2009) Hot-wire spatial resolution issues in wall-bounded turbulence. J Fluid Mech 635:103–136

Ligrani P, Bradshaw P (1987) Spatial resolution and measurement of turbulence in the viscous sublayer using subminiature hot-wire probes. Exp Fluids 5:407–417

McKeon B, Comte-Bellot G, Foss JF, Westerweel J, Scarano F, Tropea C, Meyers JF, Lee J, Cavone A, Schodl R, Koochesfahani M, Nocera D, Andreopoulos Y, Dahm J, Mullin J, Wallace J, Vukoslavcević P, Morris S, Pardyjak E, Cuerva A (2007) Springer handbook of experimental fluid mechanics, Springer, chap Velocity, Vorticity and Mach Number, pp 215–471

Pope S (2007) Turbulent flow. Spinger, New York

Smits AJ, Monty J, Hultmark M, Marusic I, Chong M (2011) Spatial resolution correction for wall-bounded turbulence measurements. J Fluid Mech 676:41–53

Tennekes, Lumley (1972) A first course in turbulence. The MIT Press, Cambridge

Vallikivi M, Hultmark M, Bailey SCC, Smits AJ (2011) Turbulence measurements in pipe flow using a nano-scale thermal anemometry probe. Exp Fluids 51(6):1521–1527

Yakhot V, Bailey S, Smits A (2010) Scaling of global properties of turbulence and skin friction in pipe and channel flows. J Fluid Mech 652:65–73